Metamaterial-enabled wireless and contactless ultrasonic power transfer and data transmission through a metallic wall

Jun Ji,[1,‡] Hyeonu Heo,[1,‡] Jiaxin Zhong,[1,‡] Mourad Oudich,[1,2,*] and Yun Jing[1,†]

[1] *Graduate Program in Acoustics, The Pennsylvania State University, University Park, Pennsylvania 16802, USA*
[2] *Université de Lorraine, CNRS, Institut Jean Lamour, Nancy F-54000, France*

(Received 18 July 2023; accepted 8 January 2024; published 30 January 2024)

Wireless ultrasonic power transfer and data transmission through a metallic wall requires a direct contact of transducers with the wall owing to the significant impedance mismatch between the surrounding fluid and the wall. Here, a pillar-based acoustic metamaterial is proposed for wireless and contactless ultrasonic power transfer and data transmission through a metallic wall by leveraging the pillar's vertical elongation mode. Experiments conducted in water demonstrate a 33-fold power transmission enhancement (from 2% to around 66%) at approximately 450 kHz through a 1-mm-thick metallic wall. Furthermore, our experiments show that a commercial light-emitting diode can be illuminated by harvesting the metamaterial-enhanced transmission of ultrasonic energy, which would not have been possible with the metallic wall alone even at an input voltage approximately 5 times greater. In addition, data transmission through the metallic wall is demonstrated by employing amplitude-shift keying modulation to transmit an image, showcasing the remarkable improvement in image quality enabled by the metamaterial. This study paves the way for a future generation of wireless and contactless ultrasonic power transfer and data-transmission applications.

DOI: 10.1103/PhysRevApplied.21.014059

I. INTRODUCTION

Wireless ultrasonic power transfer (WUPT) and data transmission (WUDT) through a metallic wall represent an exciting and rapidly advancing field of research, as metal barriers typically hinder the use of electromagnetic power transfer due to the Faraday shielding effect [1–3]. Based upon such technologies, sensors and actuators enclosed in hermetical metal containers can be wirelessly powered and can communicate with exterior environments through intact metal walls, benefiting a variety of applications in aeronautic and aerospace engineering [4,5] and nuclear engineering [6,7]. Conventionally, WUPT and WUDT utilize at least a pair of PZT (lead zirconate titanate) ultrasound transducers attached to a metal barrier. The main limitation of this approach, however, is that it requires direct contact of piezoelectric transducers with metal walls using couplants to ensure a good acoustic transmission path. The quality of couplants, such as epoxy, may degrade or even fail as operating time goes by [1], which can introduce large impedance mismatch over the acoustic-electric channel and cause the power transfer and data-transmission efficiency to rapidly decrease. Therefore, wireless and contactless ultrasonic power transfer (WCUPT) and data transmission (WCUDT) through a metallic wall is highly desirable.

Meanwhile, acoustic metamaterials (AMMs) [8] have attracted numerous research efforts in recent years due to their capability to control the propagation of sound in unconventional ways, which have led to interesting phenomena and applications such as cloaking [9–11], subwavelength imaging [12–14], and unidirectional transparency [15,16]. Despite significant advancements in acoustic metamaterials, a demonstration of an acoustic metamaterial capable of facilitating WCUPT and WCUDT through a metallic wall has yet to be achieved. On the one hand, whereas extraordinary acoustic transmission has been enabled by near-zero-density metamaterials [17,18] and acoustic evanescent waves [19–22], these designs still require small apertures for sound transmission, defeating the purpose of WUPT and WUDT. On the other hand, complementary acoustic metamaterials [23–25] have been theoretically proposed to achieve enhanced transmission noninvasively through an impedance-mismatched layer, utilizing doubly negative acoustic properties. However, experimental demonstrations of complementary acoustic metamaterials have been scarce due to the challenges in precisely prototyping either the membrane [23,26] or intricate metallic meta-atoms [25]. For the limited

*mxo5236@psu.edu
†yqj5201@psu.edu
‡These authors have equally contributed to this work.

experimental realizations of complementary acoustic metamaterials [27], though energy transmission improvements were demonstrated for weakly impedance-mismatched layers (e.g., plastic or resin barrier layers in water), the same approach may not be equally effective for through-metal-wall power transfer where relative large impedance mismatch is present. In addition to complementary metamaterials, an inversely optimized auxiliary metalens [28] has been demonstrated to assist the focusing enhancement through a 1.8-mm metallic wall in water at 200 kHz. However, the overall power transmission rate was not quantitatively analyzed. The inverse optimization method used for designing the meta-lens also may not be applicable for all general physical scenarios.

In this paper, we present a metamaterial-based approach to enable WCUPT and WCUDT through a metallic wall immersed in a strongly impedance-mismatched background medium. A deterministic method based on the band-structure theory and transmission analyses is utilized to design an ultrasonic pillar-based metamaterial. The vertical elongation mode (VEM) of the pillars is harnessed to achieve ultrasonic power transmission enhancement through the metallic wall without direct contact with transducers. This effectively addresses the notorious couplant degradation issue that is a characteristic of conventional methods in WUPT and WUDT. We numerically and experimentally demonstrate that the metamaterial, fabricated by the selective laser sintering (SLS) additive manufacturing technology, enables a 33-fold ultrasonic power transmission rate enhancement from 2% to around 66% near 450 kHz through a 1-mm-thick SUS316L plate, whose impedance is 29 times of the background medium water. In addition, a commercial red light-emitting diode (LED) is successfully lit up by harvesting the enhanced transmission of ultrasonic energy, which cannot be lit up without the metamaterial even at an input voltage that is close to 5 times greater. Benefiting from the enhanced SNR of the received signal, WCUDT is also demonstrated by transmitting an image using amplitude-shift keying (ASK) modulation at a small input voltage.

II. PILLAR-BASED ACOUSTIC METAMATERIAL

Figure 1 illustrates the working principle of the proposed WCUPT and WCUDT. A pair of co-axially aligned PZT transducers are placed on opposite sides of a metallic wall immersed in the background medium (e.g., water), working as a transmitter and a receiver, respectively. A pillar-based acoustic metamaterial, which has been studied in the past to reduce sound transmission through a thin and lightweight barrier in noise control [29,30], is now proposed to conversely enhance the power transfer through the metallic wall. The proposed pillar-based acoustic metamaterial is composed of periodically arranged pillars (with periodicity p) distributed on the metallic wall (with thickness t), as shown in the close-up views in the top-right

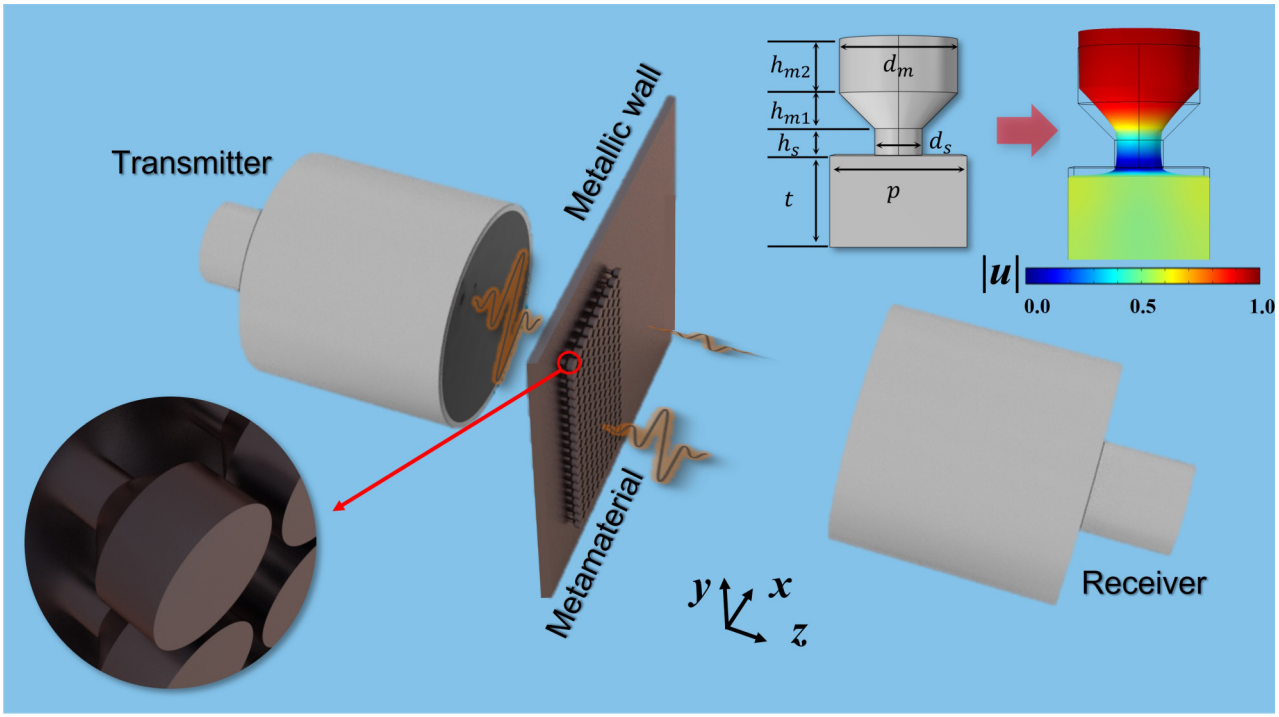

FIG. 1. Schematic of the through-metal-wall WCUPT and WCUDT system enabled by the pillar-based acoustic metamaterial. A close-up view of the metamaterial is displayed in the bottom-left corner. The displacement field of the metamaterial at VEM is shown in the top-right corner, which is the mechanism used to enhance the ultrasonic power transmission rate through the metallic wall.

and bottom-left corners of Fig. 1. Each pillar is fundamentally an acoustic spring-mass resonator, in which the large cylinder (with diameter d_m and height h_{m2}) works as a "mass" and the smaller cylinder (with diameter d_s and height h_s) works as a "spring." In this study, the pillar is assumed to be made of the same material as the wall, and is tapered with a height of h_{m1} between two cylinders in order to facilitate three-dimensional (3D) printing at a high accuracy. Once the resonant frequency of the pillar-based acoustic metamaterial is carefully tuned towards the working frequency of transducers, the ultrasonic wave generated by the transmitter can propagate through the metallic wall and excite a strong vibration of the pillars. The resonating pillars, as shown by the distribution of the normalized displacement magnitude $|\boldsymbol{u}|$ in the top-right corner of Fig. 1, will work as secondary acoustic sources to reradiate the ultrasonic wave to the other side of the wall, which would otherwise have a very limited power transmission without the metamaterial. Subsequently, the receiver can convert the metamaterial-enhanced ultrasonic signal back to electrical signal to power electronics or simply receive the signal for data transmission.

To demonstrate WCUPT, we adopt a $t = 1$ mm steel (SUS316L) wall in water and a pair of PZT transducers with a center frequency around 500 kHz. The pillar-based acoustic metamaterial is designed based on the modes observed from the calculated band structure. Figure 2(a) shows one unit cell of the proposed acoustic metamaterial distributed on the wall. The incident pressure is $p_{\text{in}} = P_{\text{in}} e^{j(-k_x x - k_y y - k_z z)} e^{j\omega t}$, in which $k_x = k \sin\theta \cos\phi$, $k_y = k \sin\theta \sin\phi$, $k_z = k \cos\theta$, and $k = \omega/c_0$. c_0 is the sound velocity in water. θ and ϕ are the polar and azimuthal angles of incidence, respectively. Figure 2(b) shows the numerical calculation (see Appendix A for details) of the complex band structure for the periodically arranged unit cells along the edges of the first irreducible Brillouin zone Γ–X–M as shown in Fig. 2(a). The size of the unit cell is $p = 1.5$ mm (half wavelength at 500 kHz), $d_s = 0.54$ mm, $d_m = 1.35$ mm, $h_s = 0.3$ mm, $h_{m1} = 0.405$ mm, and $h_{m2} = 0.615$ mm. In what follows, we will focus only

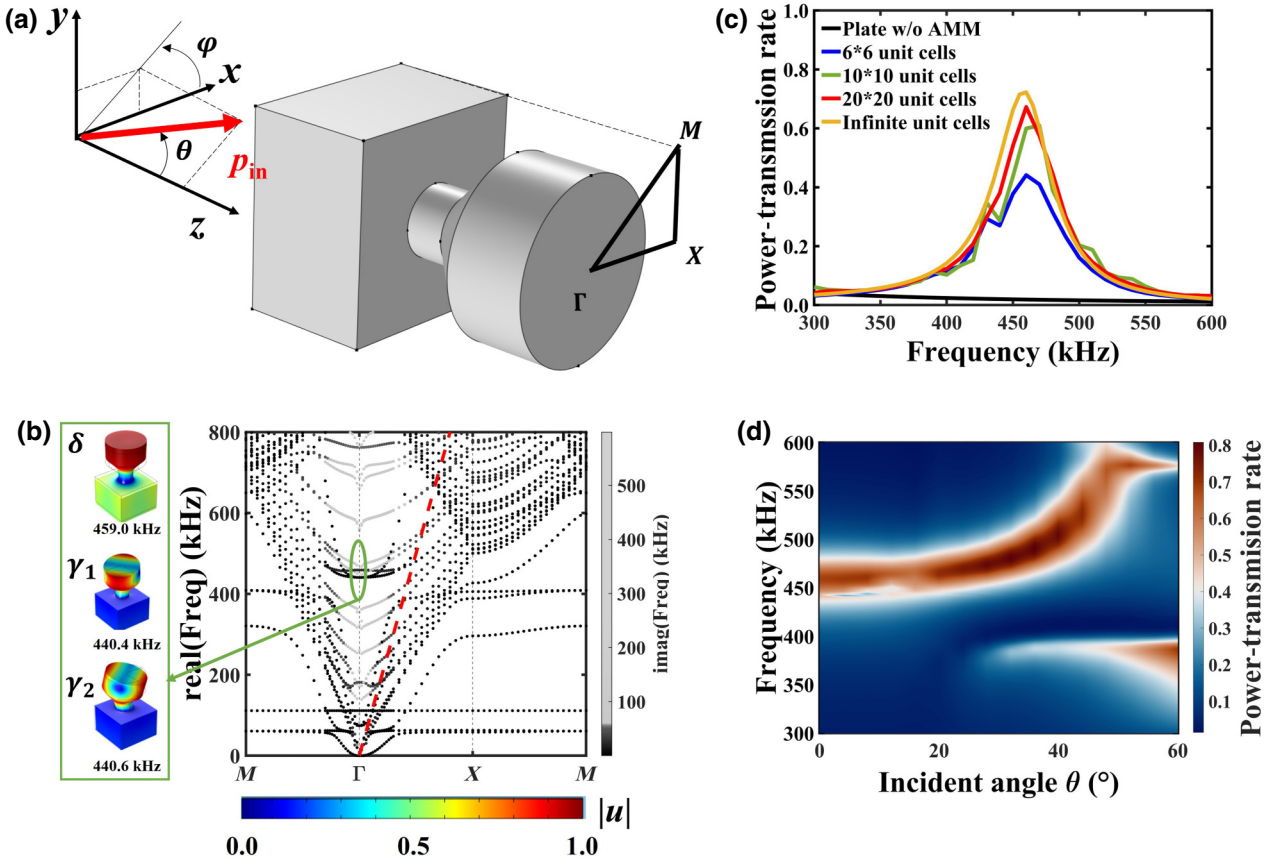

FIG. 2. Design of the pillar-based metamaterial for the through-metal-wall WCUPT and WCUDT. (a) Schematic of a periodically arranged unit cell under an incident plane wave and the first irreducible Brillouin zone. (b) The complex band structure. The real eigenfrequency is plotted on the y axis and the imaginary eigenfrequency is represented by the gray scale. The green ellipse encompasses three propagating modes corresponding to δ, γ_1, and γ_2. The distribution of the normalized displacement magnitude $|\boldsymbol{u}|$ for these modes is depicted by the color scale. The red dashed line is the sound line. (c) Power transmission rate for different numbers of unit cells under a normally incident plane wave. (d) Power transmission rate as a function of the incident angle of θ when $\phi = 0$.

on the wave dispersion along the Γ–X direction (i.e., the y component of the wave vector is zero), as the same physical behaviors can be observed for the other directions. The imaginary eigenfrequency is resulted from the plane wave radiation boundary condition applied on both incoming and outgoing planes. These modes with a large imaginary eigenfrequency are decaying fast in time (or highly evanescent in space since the speed of sound is real) and cannot transmit wave from one side of the wall to the other side. For these modes with a small imaginary eigenfrequency, the distribution of the normalized displacement magnitude $|\boldsymbol{u}|$ at the Γ point near 500 kHz is plotted to help understand the induced resonances and antiresonances from the coupling between the wall (plate) and pillars. Here, the antiresonances are modes where the vibrational amplitude at the plate becomes zero, suggesting that the transmission through the plate is not allowed, whereas the resonances correspond to a nonzero vibrational amplitude at the plate and thus have the potential to enhance transmission [31]. Near 500 kHz, while (γ_1, γ_2) is one pair of degenerate antiresonance modes, δ is a vertical elongation resonant mode with a successively stretching and compressing motion of the pillars along the vertical direction z. Based on the law of the momentum conservation, δ can be excited when the incident wave has a normal wave component (i.e., $\theta = 0$ and $\phi = 0$). The flat band frequency at which the δ mode [32] arises can be adjusted by altering the geometric parameters of the tapered pillar. Since the mode shape of δ essentially behaves like a spring-mass system, the mode frequency can be written as,

$$f \propto \sqrt{k/m} \propto \sqrt{\frac{\left(\frac{\pi}{4}d_s^2\right)E_s/h_s}{\rho_s h_{m2}\left(\frac{\pi}{4}d_{m2}^2\right) + \frac{1}{3}\rho_s h_{m1}\left(\frac{\pi d_m^2}{4} + \frac{\pi d_s^2}{4} + \frac{\pi d_m d_s}{4}\right)}}.$$

For instance, by decreasing the size of the "mass" $(h_{m2}(\pi/4)d_{m2}^2)$ or increasing the cross section $((\pi/4)d_s^2)$ of the "spring" can increase the vertical elongation mode frequency at which we enhance the transmission through the metallic barrier.

The extent to which the transmission enhancement enabled by the pillar-based acoustic metamaterial can be further assessed by numerical transmission analyses in the frequency range between 300 and 600 kHz. We first study the impact of the number of unit cells on the power transmission rate, which is evaluated under a normally incident plane wave. These results are shown in Fig. 2(c) and illustrate that the power transmission rate increases from 1.9% to 72.3% at 460 kHz when an infinite number of the designed pillar-based acoustic metamaterial units are periodically attached to a 1-mm SUS316L plate. The real eigenfrequency of 459 kHz obtained from the band-structure calculation closely aligns with the peak transmission frequency of 460 kHz observed in the transmission analyses. Typical material loss of SUS316L [33] is evaluated and it barely affects the power transmission rate according to our numerical simulations (see Note S1 in Supplemental Material [34] for details). Since the periodicity is around half of the working wavelength ($p \approx 0.46\lambda_0$), the homogenization theory [35,36] loses its effectiveness, the surface impedance analysis was used to reveal how the pillars change the effective impedance of the metallic plate as shown in Note S12 of the Supplemental Material [34]. For practical considerations, a series of numerical calculations for different finite numbers of unit cells attached on an infinitely large wall are conducted, and they show that 20×20 unit cells can achieve a power transmission rate of 67.3%, which sufficiently approaches that obtained from an infinite number of unit cells (see Note S2 in the Supplemental Material [34] for detailed simulation setup). This verifies the hypothesis of using the resonance mechanism of VEM to enhance power transmission, which is inferred from the observations in the band-structure calculation. In addition, the power transmission rate with respect to the angle of incidence is numerically evaluated, where θ varies from 0° to 60° and $\phi = 0^\circ$. Since there is no wave component on the y direction when $\phi = 0^\circ$, 20 unit cells are simulated along the x direction, and 1 unit cell is simulated along the y direction with a continuity boundary condition to reduce computational costs (see Note S3 in the Supplemental Material [34] for the detailed setup of simulations). The results are shown in Fig. 2(d) and indicate that the power transmission rate can stay at a large magnitude (more than 70%) for a wide range of angles of incidence from 0° to 60°, when excited at the proper frequency. For smaller angles of incidence though, the optimal frequency remains relatively constant and is around 460 kHz.

The generality of the pillar-based acoustic metamaterial on through-metal-wall power transmission enhancement is numerically confirmed in the background medium of air, where the impedance contrast is around 104,850. Note S4 in the Supplemental Material [34] shows that the power transmission rate is 0.00001% around 50 kHz through a 1-mm-thick SUS316L bare plate immersed in air, and it can be enhanced by at least 4 orders of magnitude to 20%, 2%, 0.6%, or 0.15%, when the loss factor of SUS316L for AMM is set as 0.0001, 0.0005, 0.001, and 0.002, respectively. Unlike the waterborne case, the power transmission rate for the airborne case is inherently ultrasensitive to the loss factor and has a narrower bandwidth, as shown in Fig. S4 within the Supplemental Material [34]. These are likely originated from the substantial impedance mismatch between the air and SUS316L, and would place a demand on advanced 3D additive metal printing to precisely control the loss factor for experimental validations.

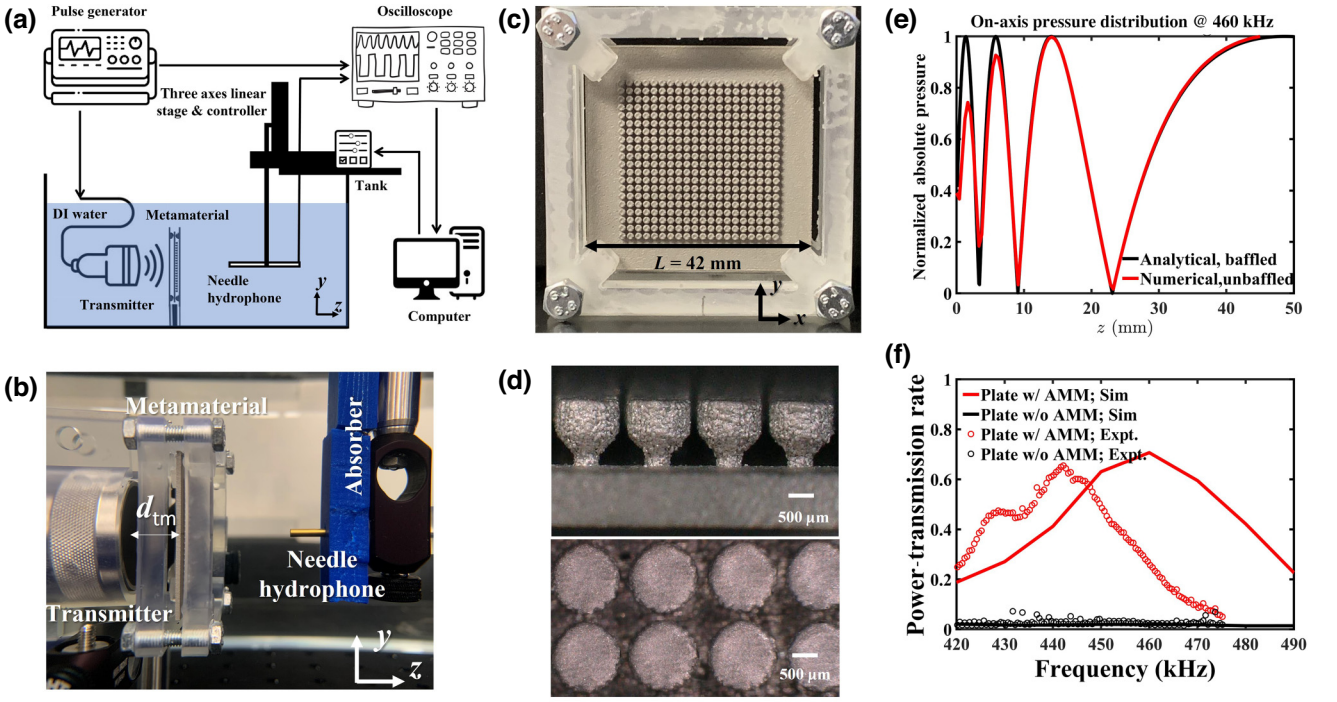

FIG. 3. (a),(b) Schematic and photo of the experimental setup. (c),(d) Fabricated plate with AMMs. (e) The on-axis pressure magnitude distribution has multiple local extremes in the near field of the piston transmitter. (f) Comparison of simulated and measured power transmission rate.

To further demonstrate the philosophy of using the pillar-based acoustic metamaterial for ultrasonic power transmission enhancement, the waterborne case is experimentally validated against numerical simulations, using the state-of-the-art 3D metal printing technology. A $42 \times 42 \times 1$ mm^3 wall ($L \times L \times t$, L is the side length) decorated with 20×20 aforementioned pillars is under an excitation from a PZT transducer with a diameter $d = 2a = 1$ inch and a central frequency around 500 kHz. Figures 3(a) and 3(b) show the schematic and photo of the experimental setup. The origin of the coordinate is set at the center of the transmitter surface and the on-axial propagating direction of the transmitter aligns with the positive z direction. The on-axial pressure field is simulated using COMSOL and compared with the analytical prediction [37] [Fig. 3(e)]. Since the on-axis pressure magnitude has multiple local extremes in the near field of the piston transmitter as shown in Fig. 3(e) (details of simulated radiation field of the transmitter are referenced to Note S6 in the Supplemental Material [34]), the plate with or without AMM is placed at the farthest maximum from the transmitter for the ease of experimental implementations, that is $d_{\text{tm}} = a(a/(m\lambda_0) - m\lambda_0/(4a)) = 14$ mm for $m = 3$ (the third extreme moving in toward the transmitter) [37] at $f_0 = 460$ kHz. However, we note that the power transmission rate is insensitive to d_{tm}, as supported by the same transmission enhancement achieved when the plate is placed at the minimal pressure location in the near field of the transmitter (details are referenced to Note S7 in the Supplemental Material [34]). Figure 3(c) shows the photo of the plate with AMM fabricated by SLS technology (see Appendix B for details), and Fig. 3(d) shows a close-up view. A needle hydrophone scans the transmitted pressure field at the other side of the plate in both x-y plane and x-z plane for three configurations ("no plate," "plate w/ AMM," and "plate w/o AMM"), as shown in Fig. 4. Details of experimental measurements are referred to Appendix C and Note S8 in the Supplemental Material [34]. The simulated and measured pressure amplitude distribution in the x-y plane is retrieved at $z = 45$ mm, which is close to the Rayleigh distance, as shown in Figs. 4(a) and 4(b). The Rayleigh distance, $L_R = d^2/(4\lambda_0)$, is the transition point between the near field and far field, and it is the preferred location for a receiving transducer to tap the maximum power from the transmitter [38]. Pressure amplitude distribution in the x-z plane is plotted at $y = 0$ mm in Figs. 4(c) and 4(d) for numerical and experimental results, respectively. The displayed pressure field is at the peak power transmission frequency, which is 442 kHz for the measurements and 460 kHz for the simulations. Then, the amount of power at the transmitted side is estimated based on the square of pressure amplitude at the surface of $z = 45$ mm, which is a reasonable approximation when transitioning to the far field (see Note S11 in the Supplemental Material for details [34]). The power transmission rate for the "plate w/AMM" and "plate w/o AMM"

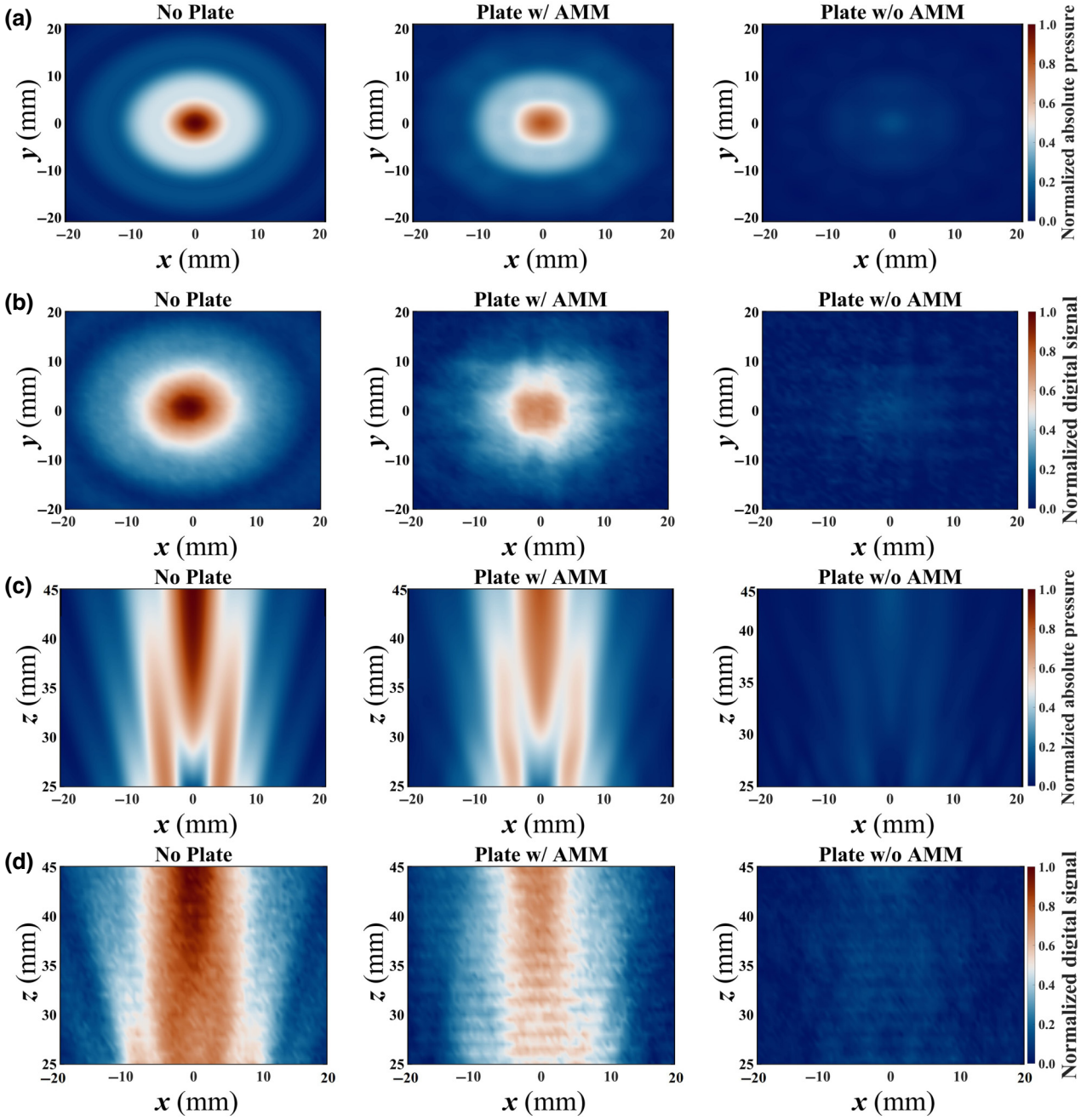

FIG. 4. The transmitted pressure field from numerical simulations (at 460 kHz) and experimental measurements (at 442 kHz) demonstrates the transmission enhancement enabled by the AMM. (a) Simulated and (b) measured pressure field in the x-y plane at $z = 45$ mm. (c) Simulated and (d) measured pressure field in the x-z plane at $y = 0$ mm. The center of the transmitter surface is set as the origin of the coordinate. For each subfigure, the pressure magnitude is normalized by the maximum value in the case of "no plate."

configurations can be obtained by normalizing the power transmission of each respective plate configuration to that of the reference "no plate" configuration. Figure 3(f) shows a comparison of simulated and measured power transmission rate for the plate with and without the AMM. The measured power transmission rate for the 1-mm bare plate is approximately 2% around 442 kHz. In contrast, with the addition of AMM on top of the plate, the measured power transmission is boosted to 65.5% at 442 Hz, with a half-power bandwidth of 33 kHz. Except the slight frequency shift (which is likely due to imperfect fabrication and details are referenced to Note S5 in the Supplemental Material [34]), a good agreement is observed between measured and simulated results, showing the expected power transmission enhancement enabled by the AMM.

III. WIRELESS AND CONTACTLESS ULTRASONIC POWER TRANSFER

With the verified capability of transmission enhancement through the metallic wall, the pillar-based acoustic metamaterial is then employed to realize a WCUPT. Figure 5(a) shows the schematic and photo of energy harvesting through the metal wall, with a larger transducer (1.5 inch diameter, 500-kHz resonant frequency) being placed at $z = 45$ mm as a receiver to collect the transmitted ultrasound power to the maximal extent. The receiver is characterized by the impedance spectrum measurement and the optimal power transfer test using a resistive load [39,40] (see Note S9 in the Supplemental Material for details [34]).

Next, we demonstrate that the enhanced ultrasonic power transmission is harvested to charge a series of capacitors and light up a commercial LED, which is otherwise impossible through a bare plate. Figure 5(b) shows the measured output signals of the receiver under an excitation of 445-kHz continuous-mode ultrasound for four different configurations: an input voltage of 4.4 Vpp on the transmitter for (i) "no plate," (ii) "plate w/ AMM", and (iii) "plate w/o AMM", as well as (iv) an input voltage of 20 Vpp on the transmitter for "plate w/o AMM." The ac collected by the receiver is not a feasible power source for most electronics. Therefore, the ac signal is rectified into a dc signal using a predesigned full-wave-bridge-rectification circuit (see Note S10 in the Supplemental Material [34] for details about the circuit design). Figure 5(c) shows the measured dc signals stored on a 220 μF during the charging process for more than 400 s until the voltage rise becomes gradual and approaches saturation. While the amplitudes of ac output signals are read as (i) 0.334, (ii) 0.264, (iii) 0.036,

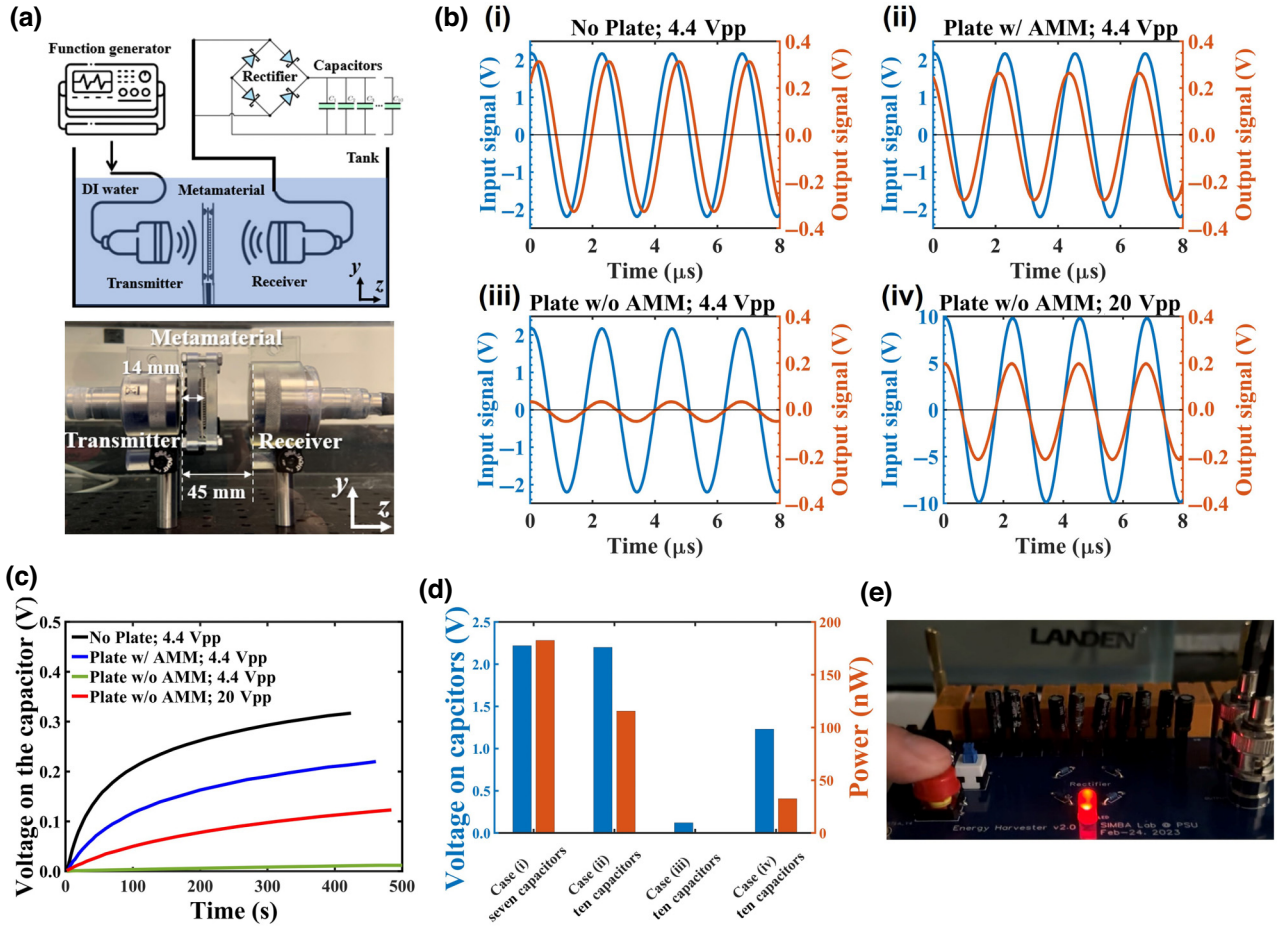

FIG. 5. Experimental results of wireless and contactless ultrasonic power transfer through a metallic wall using the pillar-based metamaterial. (a) Schematic and photo of experimental setups. The enhanced ultrasonic transmission is collected by a receiver to charge capacitors. (b) The measured output signals of the receiver under an excitation of 445-kHz continuous-mode ultrasound for four different configurations: an input voltage of 4.4 Vpp on the transmitter for (i) "no plate," (ii) "plate w/ AMM," and (iii) "plate w/o AMM," as well as (iv) an input voltage of 20 Vpp on the transmitter for "plate w/o AMM." (c) The charging time dependence of voltage on a 220 μF capacitor for the four configurations. (d) Comparison of the charged voltage and average charging power. (e) Photo showing that a commercial LED lit up in the configuration (ii).

and (iv) 0.199 V, the dc voltage on each capacitor is (i) 0.317, (ii) 0.220, (iii) 0.012, and (iv) 0.123 V. The slight voltage drop from ac to dc is mainly caused by the built-in voltage drop across the diodes of the rectifier. Considering the threshold voltage to light up a red LED is around 2 V, seven series-connected capacitors in the first configuration "no plate" collect 2.22 V, as shown in Fig. 5(d), which is enough to light up the LED. The power is also evaluated in the process, which is given by $\bar{P} = C_s V_s^2/(2T)$ [41], where C_s is the capacitance, T is the charging time, and V_s is the stored dc voltage. Thus, the energy stored on the capacitors in the first configuration is increased by 77.4 μJ in 424 s, indicating that the power output capability is 182 nW. In the second case of "plate w/ AMM", ten series-connected capacitors reaches 2.1 V with a output power of 116 nW, to successfully light up the LED as shown in Fig. 5(e). The output power of the second case is calculated as 64% of the first case, in good accordance with the measured power transmission coefficient 65.5% in Fig. 3(d). However, for the third case of "plate w/o AMM", the total voltage on ten series-connected capacitors is only 1.2 V, which is insufficient to power the LED, even when a 20-Vpp excitation was applied to the transmitter (which is the fourth case of "plate w/o AMM"). Movies that record the charging process and LED illumination are available in the Supplemental Material [34]. Details about the energy-harvesting circuit is referred to in Note S10 in the Supplemental Material [34].

IV. WIRELESS AND CONTACTLESS ULTRASONIC DATA TRANSMISSION

In addition to WCUPT, WCUDT is also demonstrated using the same setup in Fig. 5(a). Instead of using the continuous mode at a large input voltage for power transfer, burst-mode sinusoidal signals under ASK modulation are fed into the transducer at a small input voltage (25 mV) to transmit the encoded binary data. The received signals, having undergone SNR enhancement facilitated by AMM, can then be amenable to decoding. Using a string of 15-bit data [which is the signal of 15th column in Figs. 6(b)–6(e)] as an example, Fig. 6(a) showcases the encoding and decoding communication process of WCUDT: (i) The 15-bit binary signal is first embedded within start bits (100) and stop bits (001). (ii) A time-domain digital signal is generated to transmit the 21-bit binary signal using ASK modulation, and is then fed into the transmitting transducer. Here, each bit is represented by five cycles of sine waves at 445 kHz. Then 21 bits are transmitted every 0.4 ms and the communication speed is 52.5k bps. The digital power,

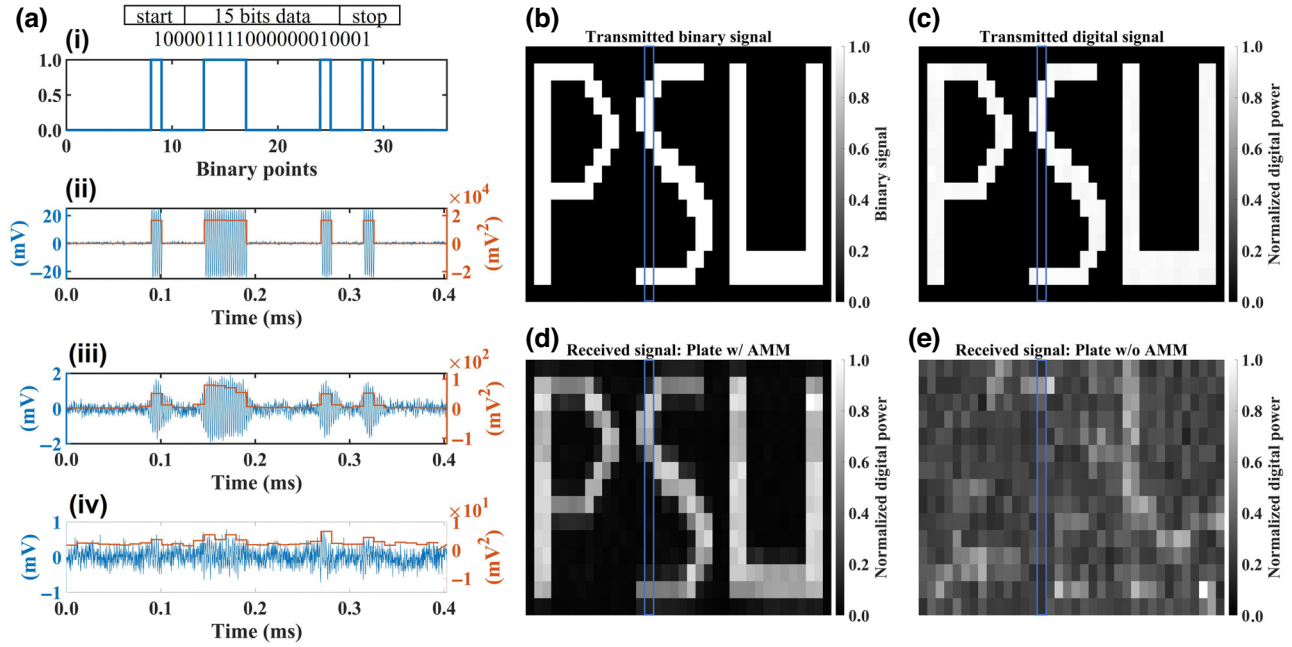

FIG. 6. Experimental results of wireless and contactless ultrasonic data transmission of a binary image of "PSU." (a) The transmission of binary data using ASK modulation: (i) a 15-bit binary signal embedded within the start bits (100) and the stop bits (001), (ii) the binary signal is transformed into digital signal before being transmitted through a PZT transducer, in which each bit is represented by five cycles of sine waves at 445 kHz, (iii) the received time-domain digital signal for "plate w/ AMM", and (iv) the received time-domain digital signal for "plate w/o AMM." For (ii)–(iv), the left axis is the digital voltage and the right axis is the digital power. (b) The original image composed of 15 × 36 pixels is encoded into binary signals of "0" and "1." (c) The transmitted digital image. (d) The received digital image for "plate w/ AMM." (e) The received digital image for "plate w/o AMM." The digital power in (c)–(e) is normalized by their respective maximum digital power. The signals in the 15th column (highlighted by blue blocks) of images in (b)–(e) are shown in (a).

which is defined as the summation of the voltage square for every five cycles of sine waves, is proposed as an algorithm to characterize the quality of the transmitted digital signal and extract data from the received digital signal. As shown by the orange curve, the line shape of the digital power for the transmitted signal agrees perfectly with the binary signal, showing the good quality of the transmitted signal. (iii) Despite a slight distortion in the received digital signal mainly caused by the frequency response of the transducer pair, the decoded signal, obtained by computing its digital power, exhibits a strong correspondence with the transmitted signal in the presence of AMM. (iv) In the absence of AMM, the transmitted signals is weaker and strongly contaminated by the noise. Consequently, the recovery of the transmitted signal from the received signal becomes challenging. Next, a more complicated binary image showing letters of "PSU" is used to demonstrate WCUDT. Figures 6(b) depicts the original image composed of 15×36 pixels, which is encoded into binary signals of "0" and "1." Figures 6(c)–6(e) are images of the digital power (normalized by their respective maximum digital power) for the transmitted signal, the received signal in the presence of AMM, and the received signal in the absence of AMM, respectively. The implementation of AMM allows for the restoration of a clear image depicting the letters "PSU." In contrast, the absence of AMM yields a noise-dominant recovered image, which necessitates an increase in the input voltage and subsequently incurs a higher power cost.

V. CONCLUSION

In summary, we have proposed a pillar-based acoustic metamaterial that enables wireless and contactless ultrasound power transfer and data transmission through a metallic plate without any openings. A deterministic method based on band-structure theory and transmission analyses is utilized to guide the design procedure. The proposed design is numerically and experimentally verified when the ambient medium is water. Our work not only expands applications for acoustic metamaterial research and 3D metal printing technology, but also sets the direction for the development of next generation of through-metal-wall ultrasonic power transfer and data transmission.

ACKNOWLEDGMENTS

Y.J. thanks the startup funds from the Pennsylvania State University.

APPENDIX A: NUMERICAL SIMULATIONS

The numerical simulations were performed using the commercial finite-element analysis software COMSOL Multiphysics V6.0. The background medium is water (air) with the density ρ_0 and speed of sound c_0 being 1000 (1.21) kg/m^3 and 1500 (343) m/s, respectively. The metallic plate and acoustic metamaterial are SUS316L with the density ρ_s, Young's modulus E_s, and Poisson's ratio ν_s being 7910 kg/m^3, 153 GPa, and 0.34, respectively. The equivalent longitudinal speed of sound of SUS316L is $c_l = \sqrt{(K_s + 4G_s/3)/\rho_s} = 5,456$ m/s, where bulk modulus $K_s = E_s/(3(1-2\nu_s))$ and shear modulus $G_s = 0.5E_s/(1+\nu_s)$. The band structure was performed using the Solid Mechanics and Pressure Acoustics modules, where the background medium of water is considered. Plane wave radiation boundary condition is applied at both incoming and outgoing planes so that a complex-valued band structure is obtained. Transmission analysis was performed using Pressure Acoustics and Solid Mechanics modules. More details are referred to in the Supplemental Material [34].

APPENDIX B: SAMPLE FABRICATIONS

The sample was fabricated using a commercial 3D printer (Metal 3D Printer ProX^{TM} DMP300) and was based on selective laser sintering (SLS) technology. The printing material is SUS316L, with a nominal resolution of 0.15 mm.

APPENDIX C: EXPERIMENTAL MEASUREMENTS

In the experiment, a $15 \times 23 \times 14$ in^3 water tank was used. It was equipped with *LC* series three axes linear stages and a three axes stepper motor controller (Newmark Systems, Inc.), travel range $400 \times 400 \times 400$ mm^3. The stages were automatically controlled through the programmed code to scan the space. The tank was filled with approximately 7 gallons of deionized water (DI water) and degassed using a water pump and vacuum pump to remove any air bubbles. Unfocused transducers (with a diameter of 1 and 1.5 in) centered at approximately 500 kHz (Olympus) were used as a transmitter and a receiver. To map the acoustic power distribution, a needle hydrophone (Onda Corps. HNR 0500) with a diameter of 2.5 mm and frequency range of 0.25–10 MHz was used. The transmitter was connected to the arbitrary waveform generator (Agilent 33250A). The receiver and hydrophone were connected to the oscilloscope (Tektronics MDO 3024 Mixed Domain Oscilloscope) to acquire and process the signals. To minimize unwanted reflections and echoes, an anechoic absorbing layer of Aptflex F28 from Acoustic Polymers Ltd was attached to the back wall and the post where the hydrophone was mounted to. Aptflex F28 is a precast polyurethane sheet that is microbubble filled, with density and wave speed similar to that of water. It exhibits high transmission loss (>30 dB/cm/MHz) and high echo reduction (>42 dB at 1 MHz). The alignment between a source, sample, and receiver was achieved by a laser alignment.

For WCUPT shown in the video [34], the transmitter was connected to the function generator Agilent 33250A, and the ac signals on the transmitter and receiver were measured by the oscilloscope. The multimeter was used to monitor the dc voltage on the capacitors. The actual voltage applied to the transmitter is twice of the value indicated on the screen of the function generator. This is because the function generator assumes a loading impedance of 50 Ω, whereas the impedance of the transmitter far surpasses the internal impedance of the function generator (50 Ω). All capacitors were connected in parallel and charged when the "SW_CHARGE" switch button was pressed down, while the "SW_WIRING" switch button was not pressed. Once the capacitors were fully charged, the "SW_CHARGE" switch was released to stop the charging process. By pressing down the "SW_WIRING" switch, all capacitors were wired in series. Finally, the "SW_LED" switch button was pressed down to power the LED. More details about the buttons on the circuit board are referred to Note S10 in the Supplemental Material [34].

For WCUDT, the discrete time-domain signal with ASK modulation was first generated in MATLAB and then imported into the arbitrary waveform generator (AWG) interface of PicoScope 5442D in order to be fed into the transmitting transducer. The ac signals on the transmitter and receiver were measured by the same oscilloscope.

[1] D.-X. Yang, Z. Hu, H. Zhao, H.-F. Hu, Y.-Z. Sun, and B.-J. Hou, Through-metal-wall power delivery and data transmission for enclosed sensors: A review, Sensors **15**, 31581 (2015).

[2] M. R. Awal, M. Jusoh, T. Sabapathy, M. R. Kamarudin, and R. A. Rahim, State-of-the-art developments of acoustic energy transfer, Int. J. Antennas Propag. **2016**, 3072528 (2016).

[3] M. G. Roes, J. L. Duarte, M. A. Hendrix, and E. A. Lomonova, Acoustic energy transfer: A review, IEEE Trans. Ind. Electron. **60**, 242 (2012).

[4] S. Sherrit, M. Badescu, X. Bao, Y. Bar-Cohen, and Z. Chang, in *Smart Structures and Materials 2005: Smart Sensor Technology and Measurement Systems*, Vol. 5758 (SPIE, 2005) p. 362.

[5] S. Sherrit, B. Doty, M. Badescu, X. Bao, Y. Bar-Cohen, J. Aldrich, and Z. Chang, in *Smart Structures and Materials 2006: Industrial and Commercial Applications of Smart Structures Technologies*, Vol. 6171 (SPIE, 2006) p. 8.

[6] H. Fu, J. Rao, M. S. Harb, and S. Theodossiades, Ultrasonic wireless power links for battery-free condition monitoring in metallic enclosures, Ultrasonics **114**, 106395 (2021).

[7] K. Sun, Y. Wu, F. Qian, H. Jung, S. Kaluvan, H. Huijin, C. Zhang, F. K. Reed, M. N. Ericson, H. Zhang, *et al.*, Self-powered through-wall communication for dry cask storage monitoring, Ann. Nucl. Energy **177**, 109306 (2022).

[8] S. A. Cummer, J. Christensen, and A. Alù, Controlling sound with acoustic metamaterials, Nat. Rev. Mater. **1**, 1 (2016).

[9] S. A. Cummer and D. Schurig, One path to acoustic cloaking, New J. Phys. **9**, 45 (2007).

[10] H. Chen and C. T. Chan, Acoustic cloaking in three dimensions using acoustic metamaterials, Appl. Phys. Lett. **91**, 183518 (2007).

[11] A. N. Norris, Acoustic cloaking theory, Proc. R. Soc. A: Math. Phys. Eng. Sci. **464**, 2411 (2008).

[12] J. Li, L. Fok, X. Yin, G. Bartal, and X. Zhang, Experimental demonstration of an acoustic magnifying hyperlens, Nat. Mater. **8**, 931 (2009).

[13] J. Zhu, J. Christensen, J. Jung, L. Martin-Moreno, X. Yin, L. Fok, X. Zhang, and F. Garcia-Vidal, A holey-structured metamaterial for acoustic deep-subwavelength imaging, Nat. Phys. **7**, 52 (2011).

[14] N. Kaina, F. Lemoult, M. Fink, and G. Lerosey, Negative refractive index and acoustic superlens from multiple scattering in single negative metamaterials, Nature **525**, 77 (2015).

[15] X. Zhu, H. Ramezani, C. Shi, J. Zhu, and X. Zhang, *PT*-symmetric acoustics, Phys. Rev. X **4**, 031042 (2014).

[16] C. Shi, M. Dubois, Y. Chen, L. Cheng, H. Ramezani, Y. Wang, and X. Zhang, Accessing the exceptional points of parity-time symmetric acoustics, Nat. Commun. **7**, 11110 (2016).

[17] R. Fleury and A. Alù, Extraordinary sound transmission through density-near-zero ultranarrow channels, Phys. Rev. Lett. **111**, 055501 (2013).

[18] J. J. Park, K. Lee, O. B. Wright, M. K. Jung, and S. H. Lee, Giant acoustic concentration by extraordinary transmission in zero-mass metamaterials, Phys. Rev. Lett. **110**, 244302 (2013).

[19] Y. Zhou, M.-H. Lu, L. Feng, X. Ni, Y.-F. Chen, Y.-Y. Zhu, S.-N. Zhu, and N.-B. Ming, Acoustic surface evanescent wave and its dominant contribution to extraordinary acoustic transmission and collimation of sound, Phys. Rev. Lett. **104**, 164301 (2010).

[20] H. Estrada, P. Candelas, A. Uris, F. Belmar, F. G. De Abajo, and F. Meseguer, Extraordinary sound screening in perforated plates, Phys. Rev. Lett. **101**, 084302 (2008).

[21] J. Christensen, L. Martin-Moreno, and F. J. Garcia-Vidal, Theory of resonant acoustic transmission through subwavelength apertures, Phys. Rev. Lett. **101**, 014301 (2008).

[22] M.-H. Lu, X.-K. Liu, L. Feng, J. Li, C.-P. Huang, Y.-F. Chen, Y.-Y. Zhu, S.-N. Zhu, and N.-B. Ming, Extraordinary acoustic transmission through a 1D grating with very narrow apertures, Phys. Rev. Lett. **99**, 174301 (2007).

[23] C. Shen, J. Xu, N. X. Fang, and Y. Jing, Anisotropic complementary acoustic metamaterial for canceling out aberrating layers, Phys. Rev. X **4**, 041033 (2014).

[24] S. R. Craig, P. J. Welch, and C. Shi, Non-hermitian complementary acoustic metamaterials for lossy barriers, Appl. Phys. Lett. **115**, 051903 (2019).

[25] C. I. Park, C. Piao, H. Lee, and Y. Y. Kim, Elastic complementary meta-layer for ultrasound penetration through solid/liquid/gas barriers, Int. J. Mech. Sci. **206**, 106619 (2021).

[26] J. Wang, F. Allein, N. Boechler, J. Friend, and O. Vazquez-Mena, Design and fabrication of negative-refractive-index metamaterial unit cells for near-megahertz enhanced acoustic transmission in biomedical ultrasound applications, Phys. Rev. Appl. **15**, 024025 (2021).

[27] L. Li, Y. Diao, H. Wu, and W. Jiang, Complementary acoustic metamaterial for penetrating aberration layers, ACS Appl. Mater. Interfaces **14**, 28604 (2022).
[28] H. Gao, Z. Gu, S. Liang, T. Liu, J. Zhu, and Z. Su, Enhancing ultrasound transmission and focusing through a stiff plate with inversely optimized auxiliary meta-lens, Appl. Phys. Lett. **120**, 111701 (2022).
[29] B. Assouar, M. Oudich, and X. Zhou, Acoustic metamaterials for sound mitigation, C. R. Phys. **17**, 524 (2016).
[30] M. Oudich, X. Zhou, and M. Badreddine Assouar, General analytical approach for sound transmission loss analysis through a thick metamaterial plate, J. Appl. Phys. **116**, 193509 (2014).
[31] M. Oudich, B. Djafari-Rouhani, Y. Pennec, M. B. Assouar, and B. Bonello, Negative effective mass density of acoustic metamaterial plate decorated with low frequency resonant pillars, J. Appl. Phys. **116**, 184504 (2014).
[32] M. Oudich, Y. Li, B. M. Assouar, and Z. Hou, A sonic band gap based on the locally resonant phononic plates with stubs, New J. Phys. **12**, 083049 (2010).
[33] M. F. Ashby, Overview no. 80: On the engineering properties of materials, Acta Metall. **37**, 1273 (1989).
[34] See Supplemental Material at http://link.aps.org/supplemental/10.1103/PhysRevApplied.21.014059 for the impact of loss factor of SUS316L on the power transmission rate in simulations; the impact of the number of unit cells on the power transmission rate in simulations; the impact of the incident angle on the power transmission rate in simulations; the power transmission enhancement through $t = 1$ mm SUS316L wall in air around 50 kHz; the impact of the fabrication errors on the resonance frequency and power transmission rate in simulations; the characteristics of the transmitter; the impact of the transmitter-sample distance on the power transmission rate in simulations; the measurement of transmitted pressure field; the characteristics of the receiver; the design of the energy-harvesting circuit; the power transmission rate in simulations and measurements; and the surface impedance analysis. Supplemental Material also contains Refs. [35–37,41], and a video showing the capacitor charging and LED powering experiment.
[35] B.-I. Popa and S. A. Cummer, Design and characterization of broadband acoustic composite metamaterials, Phys. Rev. B **80**, 174303 (2009).
[36] V. Fokin, M. Ambati, C. Sun, and X. Zhang, Method for retrieving effective properties of locally resonant acoustic metamaterials, Phys. Rev. B **76**, 144302 (2007).
[37] L. E. Kinsler, A. R. Frey, A. B. Coppens, and J. V. Sanders, *Fundamentals of Acoustics* (John Wiley & sons, New York, 2000).
[38] K. Agarwal, R. Jegadeesan, Y.-X. Guo, and N. V. Thakor, Wireless power transfer strategies for implantable bioelectronics, IEEE Rev. Biomed. Eng. **10**, 136 (2017).
[39] S. Qi, M. Oudich, Y. Li, and B. Assouar, Acoustic energy harvesting based on a planar acoustic metamaterial, Appl. Phys. Lett. **108**, 263501 (2016).
[40] M. Oudich and Y. Li, Tunable sub-wavelength acoustic energy harvesting with a metamaterial plate, J. Phys. D: Appl. Phys. **50**, 315104 (2017).
[41] L. Jiang, Y. Yang, R. Chen, G. Lu, R. Li, J. Xing, K. K. Shung, M. S. Humayun, J. Zhu, Y. Chen, *et al.*, Ultrasound-induced wireless energy harvesting for potential retinal electrical stimulation application, Adv. Funct. Mater. **29**, 1902522 (2019).